Research Article

Journal of Environmental Nanotechnology

# Green Fabrication of *Psidium guajava*-assisted Silver Nanoparticles for Efficient Photocatalytic Degradation, Broad-spectrum Antimicrobial Activity and Biomedical Applications

Anju Rani[1], Satishkumar Palanisamy[2*], M. Harish[3], Vijay R Khawale[4], M. Santhosh[5] and R. Prakash[6]

[1]Department of Physics, School of Engineering and Technology, CGC University, Mohali, PB, India
[2]Department of Mechanical Engineering, Rathinam Technical Campus, Coimbatore, TN, India
[3]Department of Aeronautical Engineering, Hindusthan Institute of Technology, Coimbatore, TN, India
[4]Department of Mechanical Engineering, Yeshwantrao Chavan Collage of Engineering, Nagpur, MH, India
[5]Department of Mechanical Engineering, Nehru Institute of Engineering and Technology, Coimbatore, TN, India
[6]Department of Science and Humanities, Rathinam Technical Campus, Coimbatore, TN, India
Received: 07.07.2026 Accepted: 06.08.2026 Published: xx.xx.xxxx
*spsatishkumar1986@gmail.com

## ABSTRACT

Green synthesis of silver nanoparticles (Ag-NPs) has emerged as a sustainable alternative to conventional chemical methods owing to its environmental compatibility and low toxicity. In this study, Ag-NPs were successfully synthesized using *Psidium guajava* leaf extract (PG) and comprehensively characterized for their structural, optical, morphological, thermal, photocatalytic, antimicrobial, and antioxidant properties. X-ray diffraction confirmed the formation of crystalline face-centered cubic silver nanoparticles with an average crystallite size of approximately 16 nm. UV–Visible spectroscopy exhibited a characteristic surface plasmon resonance band at 430 nm, while the optical band gap determined from the Tauc plot was 2.98 eV. The FTIR analysis confirmed the involvement of phytochemicals in nanoparticle reduction and stabilization. Characterization revealed quasi-spherical nanoparticles with good colloidal stability (−35.0 mV), an average hydrodynamic diameter of 85 ± 5 nm, excellent thermal stability, and a mesoporous structure with a specific surface area of approximately 96 $m^2$ $g^{-1}$. The biosynthesized Ag-NPs–PG exhibited remarkable photocatalytic activity toward Rhodamine B degradation, achieving 94.2% removal within 90 minutes under UV irradiation and maintaining 81.7% degradation efficiency after five reuse cycles. Furthermore, the nanoparticles demonstrated significant antibacterial activity against *Bacillus cereus* (20.8 mm) and *Pseudomonas aeruginosa* (18.3 mm), as well as strong antifungal activity against *Candida albicans* (22.0 mm) and *Aspergillus flavus* (19.8 mm) at 1000 µg/mL. The DPPH assay further revealed concentration-dependent antioxidant activity with a maximum radical scavenging efficiency of 91.2%. The findings demonstrate that *Psidium guajava*-mediated Ag-NPs possess photocatalytic, antioxidant, and antimicrobial properties, showing potential as eco-friendly multifunctional nanomaterials for wastewater treatment and biomedical applications.

**Keywords:** Sustainability; Antioxidant activity; Photocatalytic degradation; Rhodamine B; *Bacillus cereus*.

## 1. INTRODUCTION

Nanomaterials have become an important focus of scientific research, because of their remarkable physicochemical characteristics, including large specific surface area, enhanced catalytic efficiency, adjustable optical behavior, and diverse biological activities. Among metallic nanomaterials, silver nanoparticles (AgNPs) were widely explored because their localized surface plasmon resonance and excellent antioxidant, antimicrobial, photocatalytic, and anticancer performance, making them highly appropriate for environmental remediation and biomedical uses. However, conventional approaches for AgNP preparation generally require toxic chemicals, elevated energy input, and reaction conditions that pose environmental concerns. To overcome these limitations, green synthesis by *Psidium guajava* leaf extract has emerged as an environmentally sustainable alternative, in which naturally occurring phytochemicals function as stabilizing agents, leading to efficient formation of stable and biocompatible AgNPs.

Beyond green nanoparticle synthesis, nanostructured materials showed significant potential in environmental remediation and energy storage. Magnetically modified activated carbon prepared from teff grass straw exhibited efficient Pb(II) adsorption (Sugumar *et al.* 2024). Likewise, a grafted *Tamarindus indica* seed gum biosorbent effectively removed Cr(VI)

from aqueous media and tannery effluent, showing excellent adsorption, regeneration, and reusability performance (Sharmiladevi *et al.* 2024). In the field of electrochemical energy storage, $NiCo_2O_4$@N-C/$TiO_2$ nanocomposites exhibited high specific capacitance of 709 F $g^{-1}$ with excellent cycling stability (Vadivel *et al.* 2026). Similarly, green-synthesized Cu/$Co_3O_4$ nanocomposites delivered a specific capacitance of 345 F $g^{-1}$ and 95.3% of their capacitance after 5000 cycles, demonstrating the versatility of nanomaterials for sustainable technological applications (Ganvir *et al.* 2026).

Recent investigations have demonstrated that choice of plant significantly influences the structural and functional characteristics of AgNPs. Green-synthesized AgNPs using *Ceratonia siliqua* leaf extract produced face-centered cubic nanoparticles with crystallite sizes of 20.38 nm, while Gd-doping reduced the crystallite size to 17 nm and significantly enhanced antibacterial and antibiofilm activities through inhibition of essential bacterial enzymes (Hamadi *et al.* 2026). AgNPs synthesized using *Nothapodytes foetida* leaf extract showed FCC crystal structure with crystallite of 40.73 nm and showed potent antibacterial activity together with significant cytotoxicity against A549 and HepG2 cancer cell lines (Dharavath *et al.* 2025). Similarly, *Cyclamen libanoticum*-mediated AgNPs with a size of 17 nm showed remarkable antioxidant activity, broad-spectrum antibacterial performance, and efficient inhibition of bacterial biofilms (Hachem *et al.* 2025). Green synthesis by *Muntingia calabura* leaf extract yielded spherical AgNPs with average crystal size of 15.52 nm, which exhibited antioxidant, anti-inflammatory, antidiabetic, antibacterial, and photoluminescent properties, demonstrating the multifunctionality of plant-mediated silver nanoparticles (Vankudoth *et al.* 2022).

Besides biomedical applications, green-synthesized AgNPs have demonstrated outstanding catalytic performance toward the degradation of hazardous organic pollutants. AgNPs synthesized using *Jatropha integerrima* flower extract achieved 98% degradation of Rhodamine B dye while simultaneously exhibiting excellent antioxidant activity (Bala *et al.* 2022). Likewise, AgNPs synthesized using *Matricaria chamomilla* extract exhibited high thermal stability and efficient photocatalytic degradation of Rhodamine B with excellent catalyst reusability under ultraviolet irradiation (Alshehri and Malik, 2020). Biopolymer-coated AgNPs synthesized using starch and tea waste extract effectively degraded Rhodamine B and 4-nitrophenol while simultaneously exhibiting enhanced antibacterial and cytotoxic activities, demonstrating the advantages of surface-modified silver nanoparticles (Biswas *et al.* 2026). Similarly, *Solanum surattense*-derived AgNPs effectively degraded Rhodamine B and Acid Violet 7 dyes under direct sunlight irradiation and additionally exhibited remarkable antibacterial and anticancer activities (Mani *et al.* 2020).

AgNPs synthesized by *Acanthophyllum squarrosum* root extract achieved 98.63% photocatalytic Rhodamine B under UV irradiation and further demonstrated excellent antimicrobial, antioxidant, and cytotoxic properties at MCF-7 breast cancer (Khudhur *et al.* 2025). Plant-mediated silver nanocomposites have also been explored for enhanced environmental remediation. Reduced graphene oxide/silver nanocomposites synthesized using *Ocimum tenuiflorum* extract exhibited exceptionally adsorption capacities of 900 mg $g^{-1}$ for Rhodamine B and 970 mg $g^{-1}$ for Methylene Blue, following Langmuir isotherm with excellent regeneration efficiency (Singh and Dhaliwal, 2023). Among many medicinal plants, *Psidium guajava* has attracted increasing attention because its leaves are rich in flavonoids, phenolic acids, terpenoids, tannins and other antioxidant phytochemicals capable of efficiently reducing $Ag^+$ ions while simultaneously stabilizing the synthesized nanoparticles. Nanosilver-hydrotalcite composites synthesized using *P. guajava* leaf extract exhibited efficient Ag(I) reduction and effective antibacterial activity against *Escherichia coli* (Dam *et al.* 2024). Furthermore, green AgNPs synthesized using *P. guajava* leaf extract showed characteristic surface plasmon resonance peak at 430 nm, cubic crystalline structure, and particle size of 12 nm, together with antibacterial activity against both Gram-negative and positive bacterial strains (Islam *et al.* 2023a).

Green fabrication of silver nanoparticles, comprehensive research combining *Psidium guajava*-derived AgNP synthesis with systematic investigation of structural, optical, thermal, morphological, photocatalytic, antioxidant, antibacterial, antifungal, and anticancer properties is still rare. Accordingly, this work presents the biosynthesis of AgNPs using aqueous *Psidium guajava* leaf extract as renewable reducing and stabilizing medium. The nanoparticles were characterized by XRD, FTIR, UV–Vis spectroscopy, SEM, DLS, Zeta potential, PL, TGA, and BET techniques. Their multifunctional performance was subsequently assessed through Rhodamine B photocatalytic degradation, antioxidant, antibacterial, and antifungal studies.

## 2. MATERIALS AND METHODS

### 2.1 Materials

Healthy *Psidium guajava* leaves were obtained from Coimbatore, Tamil Nadu, India. High-purity silver nitrate served as precursor salt for biosynthesis of silver nanoparticles. Hydrogen peroxide was utilized during the photocatalytic degradation experiments as an oxidizing reagent. Other analytical-grade reagents, namely sodium chloride, ethanol, sodium carbonate, potassium chloride

and magnesium sulfate were employed directly without additional purification. Rhodamine B (RhB) dye was chosen as representative organic contaminant for photocatalytic evaluation. Distilled water was used for leaf extraction, nanoparticle preparation, washing procedures, and all photocatalytic experiments. Before each experiment, all laboratory glassware were carefully rinsed with deionized water and completely dried to minimize contamination.

## 2.2 Synthesis of Guava Leaves Extract

Freshly collected *Psidium guajava* leaves were first cleaned under flowing tap water to eliminate adhering dust and surface contaminants, followed by several washes with distilled water. Washed leaves were subsequently dried in hot-air oven maintained at 42 °C to retain heat-sensitive phytoconstituents such as phenolic compounds, flavonoids, xanthones, and anthocyanins, which play essential roles as natural reducing, surface-capping, and stabilizing agents at green fabrication of silver nanoparticles (Albadawi *et al.* 2024). A drying temperature of 42 °C was adopted because studies have shown temperatures below 50 °C help retain the antioxidant potential and heat-sensitive phytochemicals present in plant materials. After drying, leaves were ground into fine powder by electric grinder and preserved in airtight containers at ambient temperature until required. For preparing the extract, 0.50 g of the powdered leaves was mixed with 20 mL of deionized water and stirred continuously at 60 °C. The suspension was then allowed to cool naturally to room temperature and filtered by filter paper to obtain an aqueous extract, which was directly employed for the biosynthesis of AgNPs.

## 2.3 Biosynthesis of Silver Nanoparticles

Silver nitrate was employed as precursor source because of its high aqueous solubility, good chemical stability, and extensive application in green synthesis of silver nanoparticles. During reaction, $Ag^{+}$ ions generated from $AgNO_3$ were efficiently transformed into metallic silver ($Ag^{0}$) by naturally occurring phytochemicals, including phenolic compounds, flavonoids, xanthones, and anthocyanins, present in the *Psidium guajava* (PG) leaf extract, thereby promoting the formation of AgNPs (Warkad *et al.* 2026). In addition, $AgNO_3$ supplies silver ions in a controlled manner, promoting homogeneous nucleation and subsequent growth of AgNPs while remaining suitable for environmentally friendly synthesis. For nanoparticle preparation, 20 mL of *Psidium guajava* (PG) leaf extract was taken with 20 mL of a 10 mM $AgNO_3$ in a conical flask and allowed to react at ambient temperature without agitation. The reaction mixture gradually changed from a pale yellowish-brown color to dark brown, indicating the formation of AgNPs through surface plasmon resonance (SPR). The duration of nanoparticle formation was noted, and the prepared AgNP colloidal dispersion was preserved at 4 °C for characterization and application studies. The green synthesis procedure is schematically presented in Fig. 1.

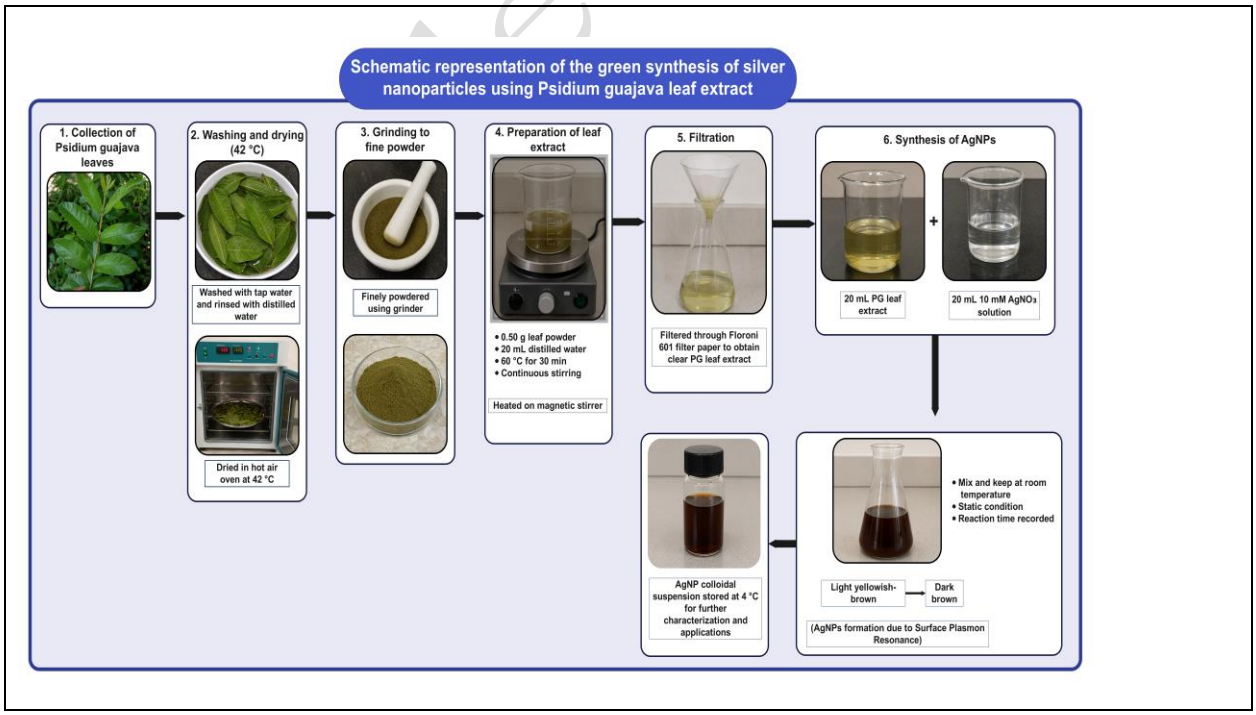


**Fig. 1: Synthesis of *Psidium guajava*-mediated AgNP**

The biosynthesis of AgNPs using *Psidium guajava* leaf extract was governed by simultaneous reduction and stabilization mechanisms driven by naturally occurring phytochemicals. The leaf extract with abundant bioactive constituents, including xanthones, flavonoids, phenolic acids, and anthocyanins, helped the formation and stabilization of silver nanoparticles (Rehan *et al.* 2026).

**Reduction Mechanism:** Phenolic and flavonoid constituents containing hydroxyl and carbonyl functional groups act as electron donors, converting $Ag^+$ ions released from $AgNO_3$ into $Ag^0$, thereby triggering the initial nucleation of nanoparticles.

**Surface Stabilization:** Oxygen-containing functional groups, including –OH and C=O, together with aromatic structures present in flavonoids and xanthones, become adsorbed on the nanoparticle surface. This surface layer suppresses particle aggregation and enhances both steric and electrostatic stability.

**Growth Regulation:** Plant-derived phytochemicals also function as natural surface-capping molecules, governing crystal growth, controlling particle dimensions and morphology, and limiting excessive aggregation. As a result, $Ag^+$ ions are efficiently transformed into stable AgNPs without the need for synthetic reducing or stabilizing reagents.

The multifunctional role of *Psidium guajava* phytochemicals as reducing, stabilizing, and capping agents provides a straightforward, sustainable, and environmentally friendly route for producing highly stable AgNPs with promising catalytic, antimicrobial, antioxidant, and biomedical applications.

## 2.4 Characterization

Optical characteristics of biosynthesized AgNPs were examined by double-beam UV–Visible spectrophotometer (Shimadzu, Japan). Absorption spectra were recorded over the wavelength range 300–800 nm using a 1-cm path-length quartz cuvette. Distilled water was employed as reference solution for baseline calibration. The measurements were performed with a spectral resolution of 1 nm, and automatic baseline correction was applied throughout the analysis (Hijazi *et al.* 2024). X-ray diffraction was performed by PANalytical X'Pert PRO instrument. Diffraction patterns were collected across 2θ range 10°–80° at a scanning speed of 2° $min^{-1}$ with a 0.02° step interval. Surface morphology was examined using a field-emission scanning electron microscope (Carl Zeiss, Germany) operated at 5.0 kV. Before SEM observation, the samples were coated with a thin gold layer to minimize surface charging (Sahare *et al.* 2025). The functional groups associated with the biosynthesized AgNPs were identified using a Perkin-Elmer Fourier transform infrared (FTIR) spectrometer by recording their infrared transmittance spectra. The colloidal stability of synthesized AgNPs was further assessed by Nano Particle/Zeta Analyzer (Japan) to determine the stability characteristics of nanoparticle suspension (Bharadwaj *et al.* 2021).

## 2.5 Photocatalytic Testing Setup

The pollutant-removal ability of the nanoparticles was examined for effluent treatment using Rhodamine B as the target organic dye because of its extensive use in textile, leather, and printing industries. Rhodamine B is a triphenylmethane dye with intense coloration, considerable chemical stability, and poor natural degradability. It also shows aquatic toxicity and may cause health effects like digestive discomfort, skin irritation, and possible carcinogenic risk. Therefore, Rhodamine B was chosen as a model contaminant to assess photocatalytic efficiency of Ag-NPs–PG for wastewater remediation. Photocatalytic tests were conducted in a batch reactor with visible-light exposure by 16 W UV lamp (254 nm) placed 15 cm from the reaction solution and operated at nominal power. Typically, 30 mg of Ag-NPs–PG were added to 100 mL of RhB dye solution in round-bottom flask. Dye degradation was monitored by UV–Vis spectrophotometry, and removal efficiency of RhB was calculated by equation 1 (Segovia-Sandoval *et al.* 2022):

$$\text{Degradation } \% = \frac{C_0 - C_t}{C_0} \times 100 \qquad \ldots (1)$$

## 2.6 Antibacterial Analysis

For antibacterial evaluation, *Pseudomonas aeruginosa* and *Bacillus cereus* were chosen as model bacterial species because of their medical and environmental relevance. *P. aeruginosa* is an opportunistic pathogen associated with urinary tract infections and wound and is well known for its biofilm-forming ability and multidrug resistance. In contrast, *B. cereus* is a foodborne bacterium responsible for gastrointestinal disorders through toxin production. Considering the increasing threat of antimicrobial resistance, these organisms were chosen to investigate the antibacterial potential of Ag-NPs–PG against clinically important pathogens. The antimicrobial activity of Ag-NPs–PG was determined by disc diffusion method employing Mueller–Hinton agar. Sterile paper discs loaded with 250, 500, and 1000 µg of Ag-NPs–PG were placed on inoculated MHA plates and incubated at 37 °C for 24 hours. The antibacterial effect was quantified by measuring the diameter of the inhibition zones surrounding each disc (Mani *et al.* 2020).

## 2.7 Antifungal Analysis

Antifungal activity of Ag-NPs–PG was investigated against *Candida albicans* and *Aspergillus*

*flavus*. *A. flavus* was chosen because it is an opportunistic pathogenic fungus capable of producing carcinogenic aflatoxins, posing serious concerns for food safety and human health. *C. albicans*, a common pathogenic yeast, was included as representative fungal strain to evaluate broad-spectrum antifungal potential of synthesized nanoparticles. Antifungal assays were carried out in potato dextrose agar (PDA) medium prepared by dissolving 2 g of dextrose, 1.5 g of agar in 100 mL of distilled water and 20 g of potato infusion. The PDA plates were supplemented with Ag-NPs–PG at concentrations of 100, 250, 500, and 1000 µg $mL^{-1}$ before inoculation with 24-hour cultures of all fungal strain (Khan *et al.* 2022).

### 2.8 Antioxidant Analysis

The free radical scavenging capacity of Ag-NPs–PG was determined by DPPH (2,2-diphenyl-1-picrylhydrazyl) assay. A 0.2 mM DPPH was prepared using methanol and combined with Ag-NPs–PG at concentrations of 100, 250, 500, 750, and 1000 µg/mL. The reaction was kept in dark at ambient temperature before measuring absorbance at 517 nm with UV–Vis spectrophotometer. Ascorbic acid was employed as positive antioxidant standard. The percentage inhibition was calculated using equation 2.

$$\text{DPPH (\% Inhibition)} = \frac{A_{\text{control}} - A_{\text{sample}}}{A_{\text{control}}} \times 100 \quad \ldots (2)$$

## 3. RESULTS AND DISCUSSION

### 3.1 X-ray Diffraction

The crystal structure and phase purity of the biosynthesized Ag-NPs–PG were investigated using X-ray diffraction. As presented in Fig. 2, the diffraction profile displayed distinct reflections at 2θ values of 44.3°, 38.1°, 64.4°, and 77.4°, which were indexed to (111), (200), (220), and (311) crystallographic planes of FCC silver, respectively.

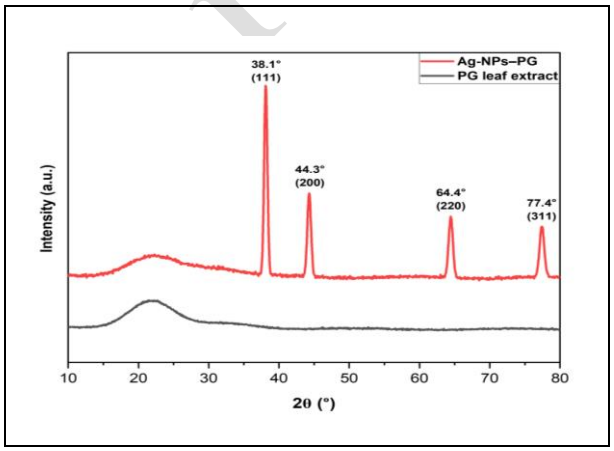


**Fig. 2: XRD profiles of PG−AgNPs**

The well-defined diffraction peaks indicate high crystalline quality of synthesized nanoparticles. Average crystallite size were estimated by applying Debye–Scherrer equation (3) (Kim *et al.* 2021):

$$D = \frac{k\lambda}{\beta \cos\theta} \quad \ldots (3)$$

Based on these parameters, the mean crystallite size of biosynthesized Ag-NPs–PG was estimated to be approximately 16 nm. Comparable findings have been reported previously, where *Psidium guajava* leaf extract-mediated AgNPs exhibited average particle size of about 12 nm with characteristic surface plasmon resonance peak near 430 nm (Islam *et al.* 2023b). To confirm that the diffraction peaks were attributed to the silver nanoparticles rather than the plant-derived components, the XRD profile of the dried *Psidium guajava* leaf extract was recorded under the same experimental conditions (Fig. 2). The diffractogram of the leaf extract exhibited a broad diffuse band centered at approximately 20–22°, which was characteristic of amorphous cellulose and other organic phytoconstituents, with no distinct crystalline reflections. This comparison demonstrates that the FCC diffraction peaks observed for Ag-NPs–PG arise exclusively from crystalline metallic silver, whereas the *Psidium guajava* extract functions as an amorphous capping and stabilizing matrix. Therefore, XRD results verify the successful biosynthesis of crystalline silver nanoparticles by *Psidium guajava* leaf extract.

### 3.2 FTIR Analysis

Infra red analysis was performed to determine the functional groups present in the plant extract and the *Psidium guajava*-derived Ag-NPs, as illustrated in Fig. 3.

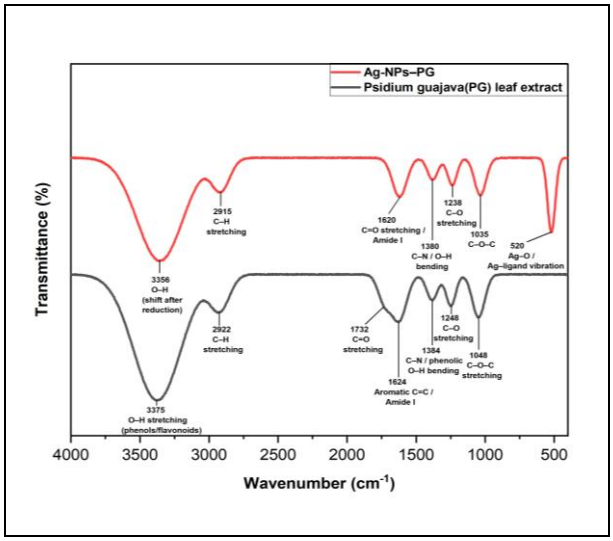


**Fig. 3: FTIR analysis of AgNPs**

The broad peak found in the spectrum of the plant extract at 3375 $cm^{-1}$ was assigned to O–H vibrations of hydroxyl and phenolic groups. The shift of this peak

to 3356 $cm^{-1}$ in the spectrum of the nanoparticles suggests involvement of these functional groups in the reduction and surface stabilization of Ag-NPs. Th peaks near 2922 and 2915 $cm^{-1}$ were associated with C–H of aliphatic moieties. The shift of the peak centered at approximately 1732 $cm^{-1}$ (C=O vibrations, leaf extract) to 1620 $cm^{-1}$ in the spectrum of Ag-NPs–PG demonstrate contribution of carbonyl-containing compounds to nanoparticle stabilization. Moreover, the peaks in the region 1384–1380 $cm^{-1}$, 1248–1238 $cm^{-1}$, and 1048–1035 $cm^{-1}$ confirm the inclusion of aromatic phytochemicals involved in the reduction and capping process. A distinct peak around 520 $cm^{-1}$ was assigned to Ag–O, indicating strong interactions between plant biomolecules and silver nanoparticles than adsorbed water molecules. The shifts in peak position and changes in peak intensity demonstrate the significant role of *Psidium guajava* phytochemicals in biosynthesis and stabilization of Ag nanoparticles.

### 3.3 UV–Vis Spectral Evaluation

Successful formation of Ag-NPs–PG was confirmed through UV–Visible absorption spectroscopy, as presented in Fig. 4a.

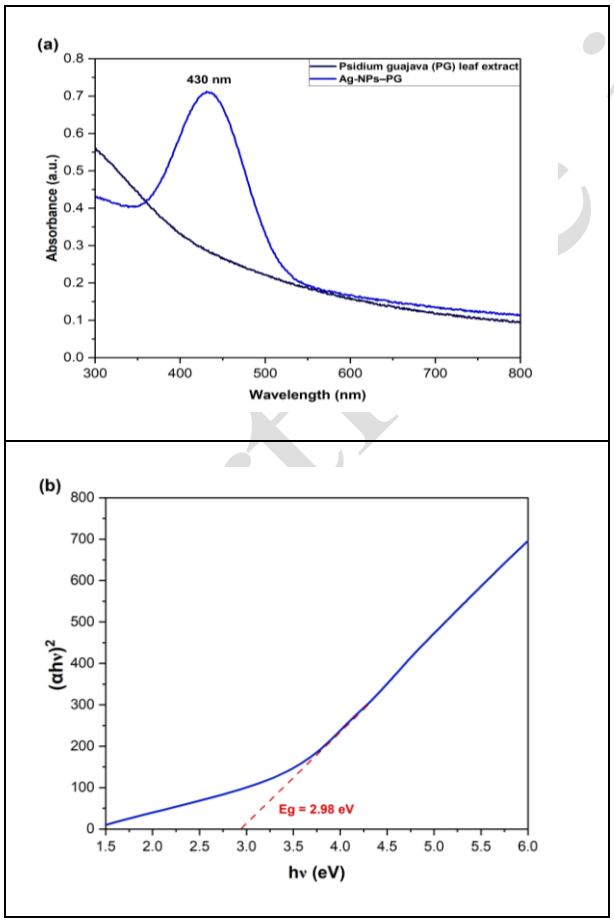


**Fig. 4: (a) AgNPs UV–Vis absorption and (b) AgNPs Tauc bandgap**

The UV–Visible spectrum of the *Psidium guajava* leaf extract exhibited broad, low-intensity absorption bands within 300–350 nm region, which are associated with π–π* electronic transitions of flavonoids, xanthones and phenolic compounds. The phytochemicals contain conjugated aromatic structures that do not exhibit surface plasmon resonance behavior. In comparison, the Ag-NPs–PG spectrum displayed distinct SPR absorption band at 430 nm, confirming the formation of metallic silver NPs. The enhanced intensity and well-defined nature of this band, together with the color change from light brown to dark brown during synthesis, verify reduction of $Ag^{+}$ ions into $Ag^{0}$ nanoparticles by the phytochemicals present in *Psidium guajava* extract. The optical band gap was further determined from Tauc plot (Fig. 4b). The linear region of $(\alpha h\nu)^2$ versus hν plot was extrapolated to band gap of 2.98 eV. This relatively lower band gap compared with bulk silver modifies the electronic characteristics. The coexistence of phytochemical absorption bands in extract and characteristic SPR peak of Ag-nanoparticles–PG confirms that biomolecules of *Psidium guajava* function both as reducing agents for $Ag^{+}$ ions and as stabilizing molecules that inhibit nanoparticle aggregation, enabling an environmentally friendly synthesis route. The measured band gap of about 2.98 eV also indicates the suitability of the synthesized Ag-NPs–PG for photocatalytic applications. A recent study has reported that plant-mediated Ag-doped ZnO nanomaterials prepared using *Cyperus rotundus* extract possessed an optical band gap of 4.20 eV, crystallite sizes of 20–25 nm, and exhibited excellent visible-light photocatalytic, gas-sensing, and antimicrobial performance (Kute *et al.* 2026).

### 3.4 Scanning Electron Microscopy

The morphology of biosynthesized Ag-NPs–PG was characterized by field-emission scanning electron microscopy. In Fig. 5a, the nanoparticles predominantly show spherical morphology with a certain degree of size variation, and average particle diameter were estimated to be 40 nm.

The observed variation in particle size is mainly associated with the diverse phytochemical composition of *Psidium guajava* leaf extract, whose bioactive constituents simultaneously act as stabilizing and reducing agents during nanoparticle formation. Differences in the local abundance of flavonoids, phenolic compounds, and xanthones influence reduction kinetics of $Ag^{+}$ ions, resulting in nanoparticles with non-uniform dimensions. As illustrated in Fig. 5b, a few regions also display irregularly shaped particles and clustered aggregates. Such aggregation is commonly encountered in plant-mediated nanoparticle synthesis, particularly during SEM sample preparation, where solvent removal promotes particle–particle interactions. Similar morphological characteristics have been reported

for biosynthesized AgNPs, in which naturally occurring phytochemicals perform dual roles as capping and reducing agents, giving rise to different nucleation behaviors and particle morphologies (Islam *et al.* 2023a).

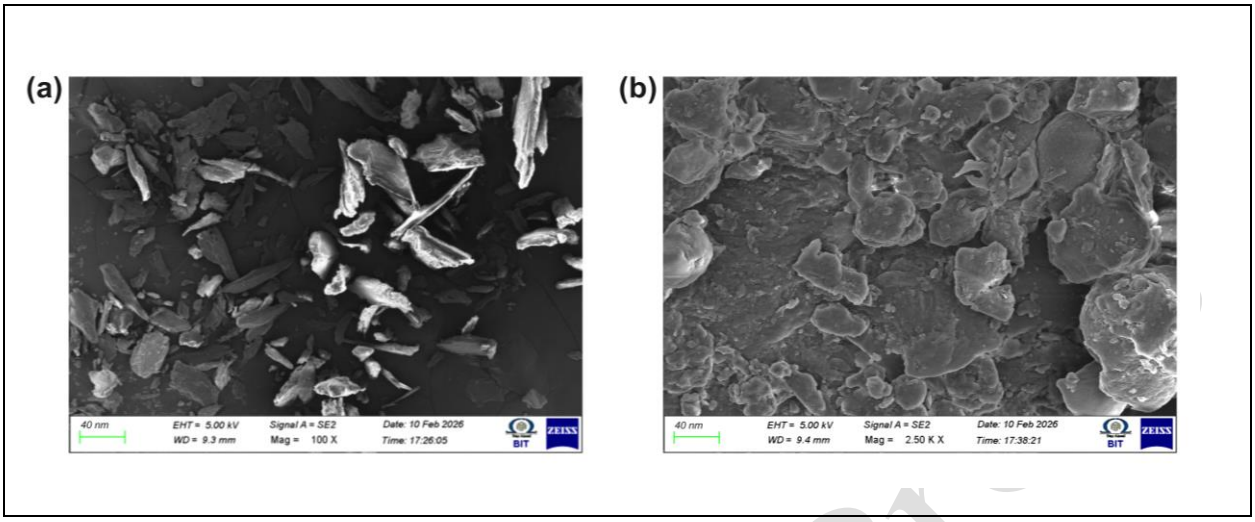


**Fig. 5: a–b SEM micrographs of AgNPs**

## 3.5 DLS and Zeta Potential

Dynamic light scattering was employed to determine the hydrodynamic size distribution and colloidal stability of Ag-NPs–PG dispersed in an aqueous medium, as presented in Fig. 6a.

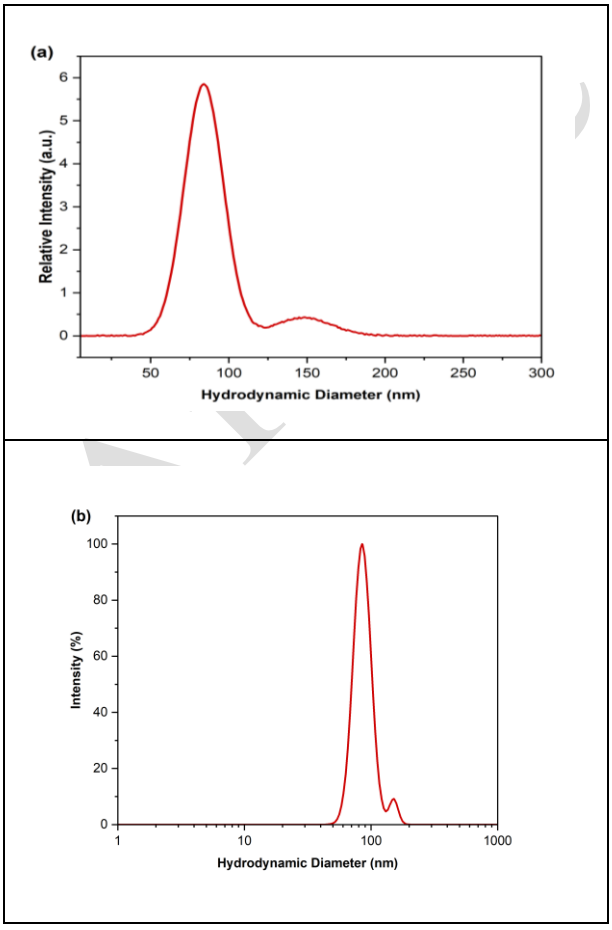


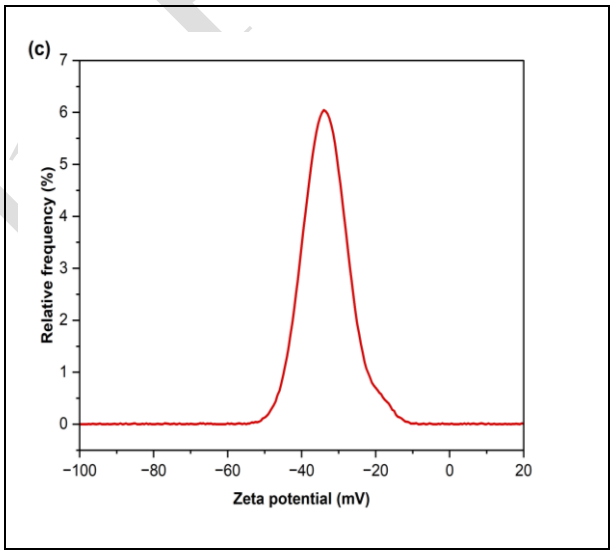


**Fig. 6: (a) Hydrodynamic diameter analysis, (b) Particle size distribution and (c) Zeta potential distribution**

Average hydrodynamic diameter (Z-average, Dh) of Ag-NPs–PG was determined to be 85 ± 5 nm, which is larger than the particle size obtained from FESEM (approximately 10–70 nm). This difference is expected because DLS measures the hydrated particle, including the metallic core, the surrounding phytochemical layer, and associated solvent shell. The measured PDI of 0.27 ± 0.02 indicates relatively uniform particle size distribution, which is characteristic of plant-mediated nanoparticle synthesis where multiple phytochemicals participate in reduction and stabilization. The intensity-based particle size profile (Fig. 6b) exhibited a predominantly single distribution centered between 80 and 90 nm, with a minor peak at 151 nm, suggesting inclusion of small fraction of aggregated

particles. Colloidal stability of Ag-NPs–PG was further assessed through zeta potential analysis (Fig. 6c), which yielded a value of −35.0 mV. This highly negative surface charge provides strong electrostatic repulsion particles, minimizing aggregation and improving suspension stability. Generally, zeta potential greater ±30 mV shows good colloidal stability, whereas the values around ±20 mV provide sufficient electrostatic and steric stabilization. A recent study reported crystallite sizes of 12–22 nm and a zeta potential of −31.50 mV for silver nanoparticles synthesized by *Bacopa monnieri* leaf extract, which showed size-dependent photoluminescence emissions in the 390 nm and 580–620 nm regions (Sivalingam, 2026). The combined findings from DLS, FESEM, zeta potential analyses demonstrate that *Psidium guajava*-mediated Ag nanoparticles possess nanoscale dimensions, excellent colloidal stability, and desirable characteristics for biomedical and photocatalytic applications.

### 3.6 Thermal Stability Analysis

The thermal behavior of biosynthesized Ag-NPs–PG was investigated by thermogravimetric analysis (TGA) over the temperature range 30–900 °C, as illustrated in Fig.7.

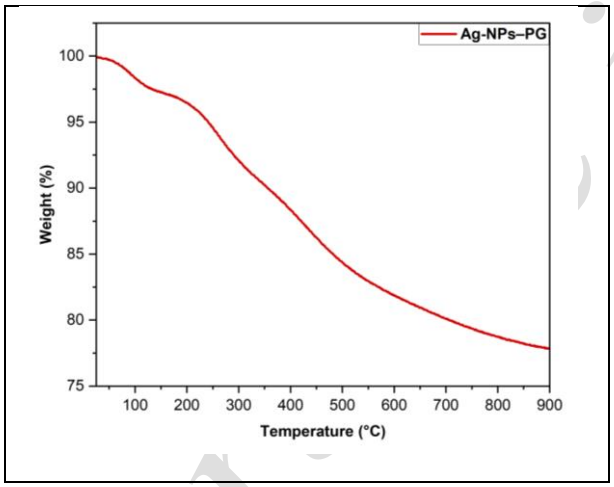


**Fig. 7: Thermal stability of AgNPs**

The TGA profile revealed three stages of mass loss. The first stage, observed below 150 °C was attributed to elimination of weakly bound water molecules and physically adsorbed moisture. The second stage, extending from 200 to 500 °C, corresponded to the decomposition of thermally unstable phytochemicals derived from the *Psidium guajava* leaf extract, including flavonoids, polysaccharides and phenolic compounds, which participate in stabilization and reduction of Ag-NPs. A gradual weight loss was further observed between approximately 500 and 900 °C. This prolonged decomposition is associated with lignin-rich constituents and polyphenolic residues that undergo thermal degradation or oxidation over a broad temperature range, releasing CO, $CO_2$, and other volatile products. The TGA curve showed total weight loss of 22%, with a residual mass of about 78% at 900 °C, indicating that the phytochemicals from *Psidium guajava* form a protective organic capping that decomposes progressively during heating, making the crystalline silver nanoparticles remain thermally stable upto 900 °C.

### 3.7 Surface Area Characterization

An $N_2$ adsorption–desorption isotherm of the biosynthesized Ag-NPs–PG (Fig. 8a) exhibited the typical characteristics of type IV mesoporous isotherm with H3 hysteresis loop. The BET analysis estimated a surface area of 96 $m^2\ g^{-1}$ for synthesized Ag-NPs. The BJH pore size distribution curve (Fig. 8b) indicated a dominant pore diameter of approximately 13.5 nm, together with a minor pore population centered around 5–6 nm, confirming the mesoporous nature of the biosynthesized nanoparticles.

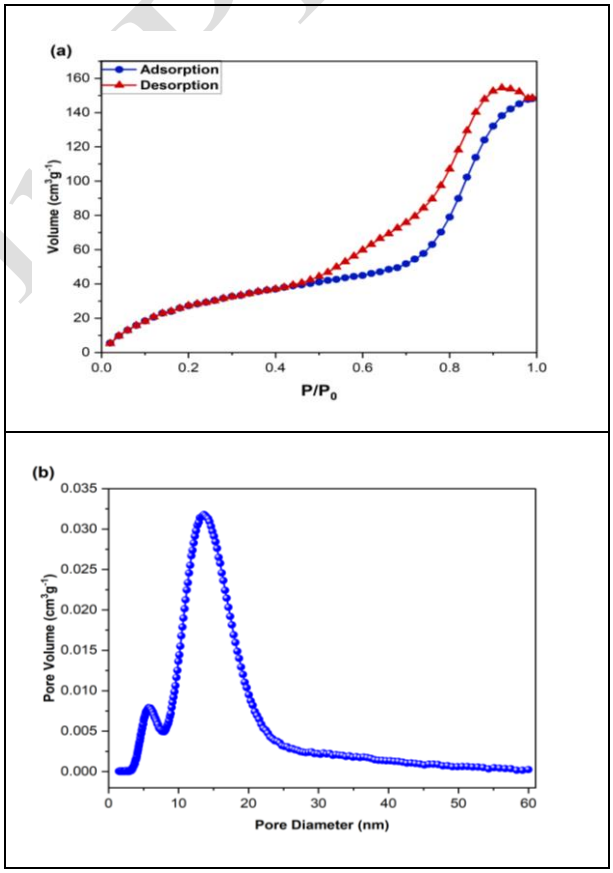


**Fig. 8: (a) Nitrogen adsorption isotherms and (b) Pore size distribution**

### 3.8 Photocatalytic RB Dye Removal

The photocatalytic activity of Ag-NPs–PG was investigated using Rhodamine B dye as the pollutant under visible-light irradiation. The catalyst–dye suspension was magnetically stirred in dark for 30

minutes to establish adsorption–desorption equilibrium. The time-dependent UV–Visible absorption of RhB degradation with inclusion of Ag-NPs–PG during 0–90 min of visible-light exposure is shown in Fig. 9a.

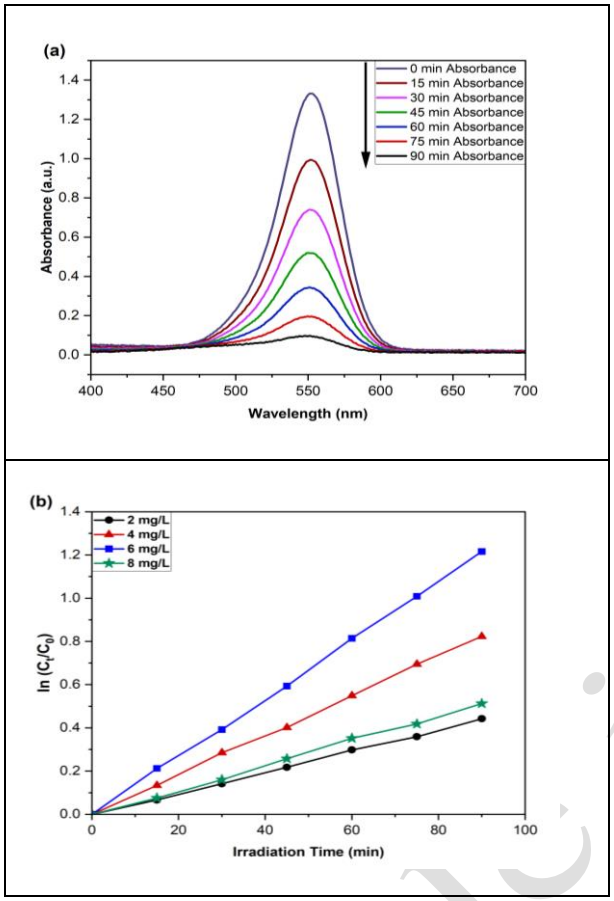


**Fig. 9: (a) RB Photodegradation under UV and (b) Photodegradation kinetic analysis**

Furthermore, the control study demonstrated that direct photodegradation of RhB under visible-light irradiation was minimal (<5%), whereas the Ag-NPs–PG photocatalytic system achieved approximately 93–94% dye removal with 90 minutes, highlighting the essential role of the catalyst. The characteristic absorption peak of RhB at around 550 nm decreased with increasing irradiation duration, confirming degradation of dye molecules. The degradation behavior was analyzed by Langmuir–Hinshelwood kinetic model, where RhB molecules are initially adsorbed onto the surface of Ag-NPs–PG and subsequently decomposed by reactive oxygen species (ROS), including •OH, $O_2^{\bullet-}$, and $h^+$, during visible-light irradiation. The L–H rate equation is expressed by equations 4 and 5(Gaddala *et al.* 2025):

$$r = -\frac{dc}{dt} = \frac{kKC}{1+KC} \quad \ldots (4)$$

$$\ln\frac{C_0}{C_t} = k_{app}t \quad \ldots (5)$$

The linear relationship obtained from the plot $\ln(C_0/C_t)$ *vs*. irradiation duration (Fig. 9b) demonstrated good conformity with the kinetic model, indicating that photocatalytic degradation of RhB by Ag-NPs–PG follows pseudo-first-order kinetics. Comparable kinetic behavior has been reported for organic dye degradation using biosynthesized silver NPs and metal-based photocatalysts, supporting suitability of model for the present system (Sharma *et al.* 2023). These findings suggest that the reaction is predominantly governed by surface adsorption, where the phytochemical-capped AgNP surface offers active sites for RhB adsorption, photoinduced holes and electrons to generate ROS that efficiently oxidize the dye molecules.

## 3.9 Process Parameter Optimization

To gain an understanding of photocatalytic behavior of Ag-NPs–PG, the key experimental variables were systematically investigated, including catalyst loading, presence of sacrificial reagents and influence of different electrolytes like phenol, citric acid, formic acid, oxalic acid, and EDTA.

### 3.9.1 Influence of Catalyst loading

Rhodamine B degradation was investigated by varying the Ag-NPs–PG loading from 10 to 60 mg/100 mL while maintaining a constant solution pH. As illustrated in Fig. 10, a catalyst dose of 30 mg/100 mL produced maximum degradation of approximately 94.2% after 90 minutes of UV-light irradiation.

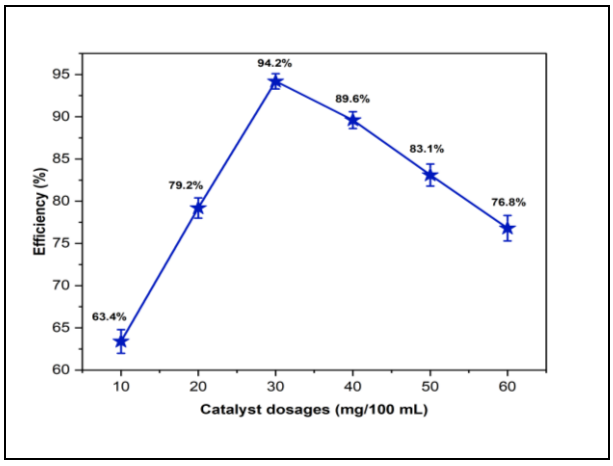


**Fig. 10: Catalyst loading on RB degradation**

The loadings of 10 mg/100 mL and 20 mg/100 mL achieved degradation efficiencies of 63.4% and 79.2%, respectively, because of the limited availability of active surface sites and reactive oxygen species. Increasing the catalyst loading to 40**,** 50, and 60 mg/100 mL resulted in degradation efficiencies of 89.6%, 83.1%, and 76.8%, respectively. The reduction in photocatalytic performance on higher catalyst dosages was attributed to particle agglomeration and increased light scattering,

which decrease the effective catalytic surface area and limit interaction between catalyst and dye molecules. Boddu *et al.* (2024) reported that plant-derived silver nanoparticles exhibited efficient Rhodamine B degradation, reaching a maximum removal efficiency of 93.56% under optimized reaction conditions with a catalyst concentration of 3 g/L. These results demonstrate that careful optimization of the Ag-NPs–PG dosage is essential to obtain the highest photocatalytic degradation.

#### 3.9.2 Influence of Sacrificial Agents

The reagents on photocatalytic degradation were investigated by 30 mg/100 mL of Ag-NPs–PG at pH 7 (Fig. 11). Citric acid and EDTA were employed as oxalic acid, formic acid and hole ($h^+$) scavengers, acted as both •OH scavengers and hole, while phenol were used as a hydroxyl radical (•OH) scavenger.

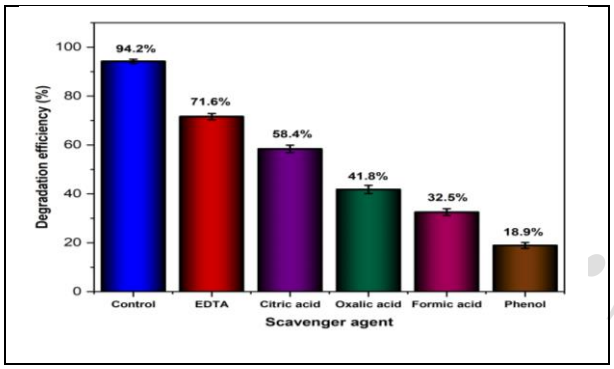


**Fig. 11: Scavenger effect on photodegradation**

Addition of sacrificial reagents markedly influenced photocatalytic degradation efficiency, demonstrating the participation of ROS in degradation pathway. In the absence of scavengers (control), the Ag-NPs–PG photocatalytic system achieved a degradation efficiency of approximately 94.2%. Among the investigated scavengers, EDTA and citric acid resulted in comparatively higher degradation efficiencies of approximately 71.6% and 58.4%, respectively. Lower degradation efficiencies were obtained in the presence of formic acid (32.5%), phenol (18.9%) and oxalic acid (41.8%), after 90 minutes of visible-light irradiation. In contrast, relatively higher degradation efficiencies recorded with EDTA and citric acid indicate that photogenerated holes play a less prominent role. The intermediate effects of oxalic acid and formic acid further suggest that both holes and •OH radicals contribute to the overall mechanism.

#### 3.9.3 Influence of Electrolytes

The influence of commonly encountered inorganic salts, namely $Na_2CO_3$, $MgSO_4$, NaCl, and KCl, on photocatalytic degradation of Rhodamine B was investigated over a concentration range of 0–7 wt%, as presented in Fig. 12.

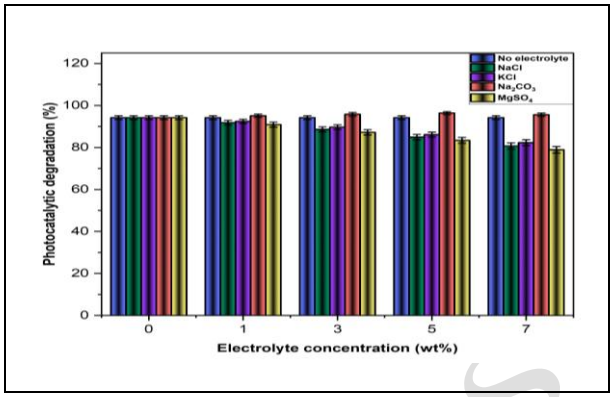


**Fig. 12: Electrolyte influence on photodegradation**

The addition of chloride- and sulfate-containing salts, such as $MgSO_4$ and NaCl, decreased the photocatalytic degradation from 94.0% to 79.0% and 94.0% to 81.0%. Conversely, the incorporation of $Na_2CO_3$ produced a slight enhancement in dye degradation, probably because of its favorable effect on generation of ROS. Although degradation efficiency varied with the type of electrolyte present, Ag-NPs–PG consistently exhibited high photocatalytic performance under all investigated conditions.

### 3.10 Reusability Evaluation

Recycling performance of Ag-NPs–PG was evaluated by 5 successive photocatalytic cycles carried out under same experimental conditions, in Fig. 13.

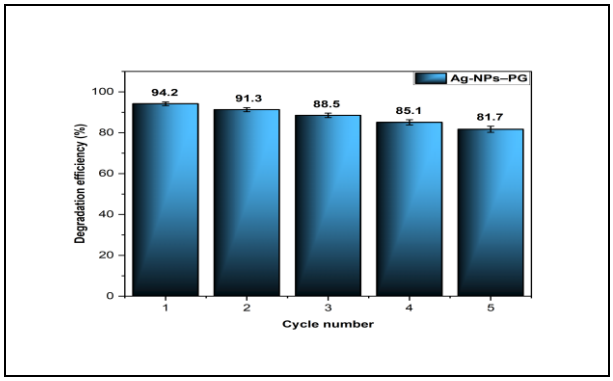


**Fig. 13: Recyclability of AgNPs**

Photocatalytic degradation declined 94.2% in first cycle to 81.7% after fifth cycle. The degradation efficiencies for the second, third, and fourth cycles were 91.3%, 88.5%, and 85.1%, respectively. This slight loss in activity was primarily associated with deposition of degraded by-products on nanoparticle surface, which partially block the available active sites. Despite this decrease, Ag-NPs–PG maintained high photocatalytic performance throughout repeated cycles, demonstrating excellent stability, reusability, and potential for practical environmental remediation.

## 3.11 Photocatalytic Degradation Pathway

The photocatalytic reaction was initiated by adsorption of Rhodamine B molecules onto the surface of Ag-NPs–PG, where many active sites facilitate effective dye–catalyst interaction. Under visible-light irradiation, Ag-NPs–PG/$H_2O_2$ system promotes generation of ROS through decomposition of hydrogen peroxide, producing highly oxidative hydroperoxyl (HOO•) and hydroxyl (•OH) radicals. These reactive radicals readily attack adsorbed RhB molecules, destroying chromophore structure and converting them into smaller intermediates, which are ultimately mineralized into $CO_2$ and $H_2O$. In addition, the phytochemical coating from *Psidium guajava* leaf extract enhances dye adsorption and improves charge separation, thereby suppressing electron–hole recombination and sustaining continuous radical formation.

## 3.12 Bioactivity Evaluation

### 3.12.1 Antibacterial Activity Assessment

The antibacterial performance of Ag-NPs–PG was systematically evaluated against Gram-positive bacterium *Bacillus cereus* and Gram-negative bacterium *Pseudomonas aeruginosa* by agar well diffusion technique. Representative photographs of inhibition zones produced by Ag-NPs–PG are presented in Fig. 14a and Fig. 14b, while the corresponding antibacterial data are summarized in Table 1.

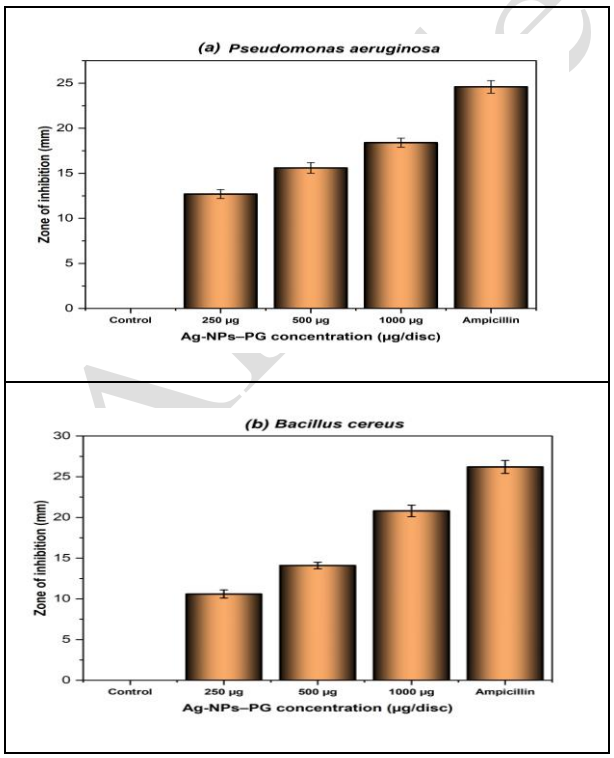


**Fig. 14: (a) *Pseudomonas aeruginosa* inhibition zone and (b) *Bacillus cereus* Inhibition Zone**

**Table 1. Antibacterial inhibition zone analysis**

| Organisms | Zone of Inhibition Sample (µg/mL) 1000 (mm) | 500 (mm) | 250 (mm) | Std |
|---|---|---|---|---|
| *Bacillus cereus* | 20.8 ± 0.5 | 14.1± 0.4 | 10.6 ± 0.5 | 26.2 ± 0.8 |
| *Pseudomonas aeruginosa* | 18.3 ± 0.5 | 15.6 ± 0.5 | 12.6 ± 0.4 | 24.8 ± 0.7 |

The experimental findings demonstrate that Ag-NPs–PG possess antibacterial activity against both Gram-positive and negative bacterial strains. The Ag-NPs–PG produced largest inhibition zones, indicating superior antimicrobial effectiveness. This improved antibacterial performance was attributed to combined action of intrinsic antimicrobial properties of silver nanoparticles and the increased generation of ROS, which together contribute to efficient bacterial cell inactivation.

### 3.12.2 Antifungal Activity Assessment

The antifungal activity of the biosynthesized Ag-NPs–PG was evaluated against *Candida albicans* and *Aspergillus flavus*. Representative images of the inhibition zones are presented in Fig. 15a and Fig. 15b, while corresponding antifungal results are summarized in Table 2.

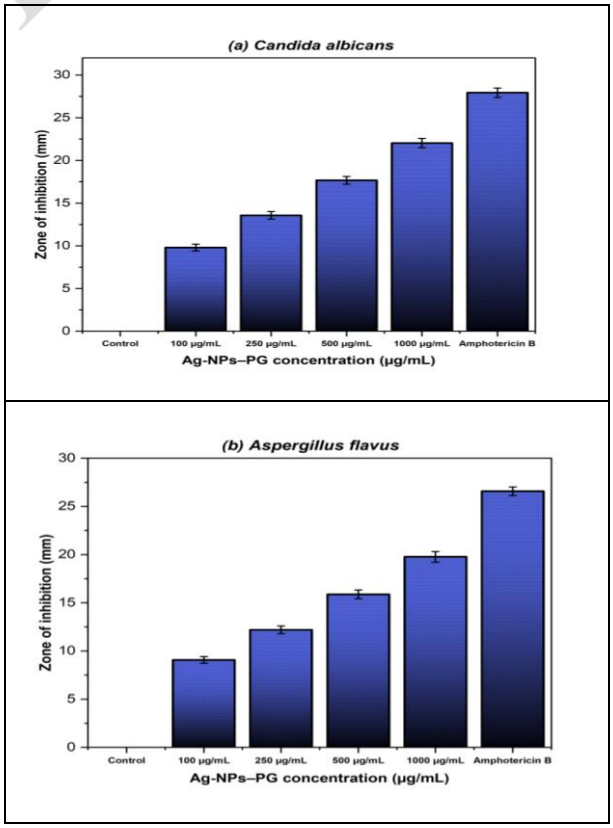


**Fig. 15: (a) *Aspergillus flavus* growth inhibition and (b) *Candida albicans* growth inhibition**

**Table 2. Antifungal inhibition zone analysis**

| S. No. | Test Organism | Test Sample | Zone of Inhibition | | | | |
|---|---|---|---|---|---|---|---|
| | | | $\frac{1000\mu g}{ml}$ | $\frac{500\mu g}{ml}$ | $\frac{250\mu g}{ml}$ | $\frac{100\mu g}{ml}$ | PC |
| 1. | *Aspergillus flavus* | Ag-NPs–PG | 19.8 ± 0.4 | 15.8 ± 0.4 | 12.2 ± 0.3 | 9.0 ± 0.3 | 26.5 ± 0.5 |
| 2. | *Candida albicans* | Ag-NPs–PG | 22.0 ± 0.5 | 17.7 ± 0.4 | 13.6 ± 0.4 | 9.8 ± 0.3 | 27.8 ± 0.6 |

Ag-NPs–PG displayed a concentration-dependent antifungal response, with the greatest inhibition recorded at 1000 µg/mL and the lowest activity observed at 100 µg/mL. *Candida albicans* and *Aspergillus flavus* were highly susceptible to synthesized nanoparticles, showing antifungal activity comparable to that of the reference drug, amphotericin B. The remarkable antifungal performance of Ag-NPs–PG showed combined effects of phytochemical constituents and silver nanoparticles from *Psidium guajava* as surface-capping agents. Nanoparticles are believed to disrupt fungal cell walls and membranes, resulting in leakage of intracellular components and loss of cellular integrity. Furthermore, the phytochemical coating, enriched with phenolic compounds, flavonoids, and xanthones, promoting the formation of ROS with oxidative damage within fungal cells. Concentration-dependent inhibition also suggests that higher nanoparticle dosages provide a greater number of active sites for interaction with fungal pathogens. These results demonstrate the strong antifungal capability of Ag-NPs–PG and support their potential application in antifungal and biomedical fields.

### 3.12.3 Antioxidant Activity Assessment

Reactive oxygen species and free radicals produced at normal biological metabolism are major factors responsible for oxidative stress and development of different diseases. Antioxidants minimize this damage by scavenging free radicals, thereby protecting cellular components from oxidative injury. The antioxidant capacity of Ag-nanoparticles–PG was assessed by 2,2-diphenyl-1-picrylhydrazyl free radical scavenging. Absorbance was recorded at 517 nm, standard wavelength used to evaluate DPPH radical reduction. Although complete UV–Visible spectra were not obtained, the scavenging activity measured at 517 nm provides a reliable assessment of antioxidant performance of synthesized nanoparticles. Chirumamilla *et al.* (2023) reported green-synthesized Ag nanoparticles prepared by *Solanum khasianum* leaf, which exhibited characteristic UV–Visible absorption peak at 440 nm together with remarkable DPPH radical scavenging, antidiabetic, antibacterial, and concentration-dependent anticancer activities. As illustrated in Fig. 16 and in Table 3, Ag-NPs–PG showed remarkable free radical scavenging activity over the entire concentration range, with antioxidant activity increasing in concentration-dependent manner. Highest scavenging efficiency of 91.2% was achieved at 1000 µg $mL^{-1}$, while values of 87.6%, 82.7%, 57.8%, and 35.2% were recorded at 750, 500, 250, and 100 µg $mL^{-1}$, respectively.

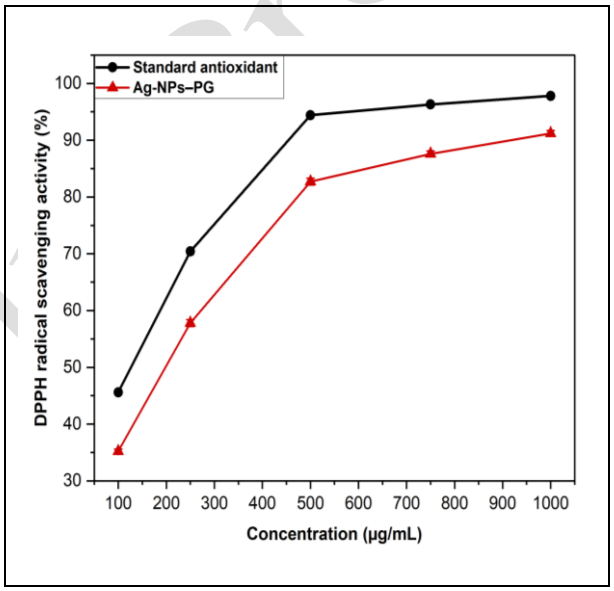


**Fig. 16: Free radical scavenging analysis**

**Table 3. Antioxidant activity of AgNPs**

| S. No. | Concentration | Mean | Mean |
|---|---|---|---|
| 1. | 100 | 45.6 | 35.2 |
| 2. | 250 | 70.4 | 57.8 |
| 3. | 500 | 94.4 | 82.7 |
| 4. | 750 | 96.3 | 87.6 |
| 5. | 1000 | 97.8 | 91.2 |

These findings demonstrate that the biosynthesized Ag-NPs–PG exhibit excellent antioxidant activity, primarily due to the bioactive phytochemicals from *Psidium guajava* leaf extract that remain attached to the nanoparticle surface as functional capping molecules.

## 4. CONCLUSION

Green-synthesized Ag-NPs–PG were successfully fabricated by *Psidium guajava* leaf extract through simple and eco-friendly method. X-ray diffraction confirmed formation of crystalline FCC silver nanoparticles with an average crystallite size of 16 nm. UV–Visible analysis showed a characteristic SPR peak at 430 nm and the optical band gap was 2.98 eV. Other analyses such as, FESEM, DLS, zeta potential, TGA, and BET revealed quasi-spherical morphology, good colloidal stability (−35.0 mV), excellent thermal stability, and a mesoporous structure with specific surface area of approximately 96 $m^2$ $g^{-1}$. The Ag-NPs–PG exhibited outstanding photocatalytic performance, achieving 94.2% Rhodamine B degradation within 90 minutes and retaining 81.7% efficiency after five reuse cycles. The nanoparticles demonstrated significant antibacterial, antifungal, and antioxidant activities, with maximum inhibition zones of 20.8 mm (*Bacillus cereus*), 18.3 mm (*Pseudomonas aeruginosa*), 22.0 mm (*Candida albicans*), and 19.8 mm (*Aspergillus flavus*), together with 91.2% DPPH radical scavenging activity at 1000 µg/mL. These findings demonstrate that *Psidium guajava*-mediated Ag-NPs are promising multifunctional nanomaterials for wastewater treatment, antimicrobial applications, and biomedical research.

## FUNDING

This research received no specific grant from any funding agency in the public, commercial, or not-for-profit sectors.

## CONFLICTS OF INTEREST

The authors declare that there is no conflict of interest.

## COPYRIGHT



## REFERENCES

Albadawi, E. A., Musa, E. N. A., Ghaban, H. M., Ebrahim, N. A., Albadrani, M. S. and El-Tokhy, A. I., Eco-friendly green synthesis of silver nanoparticles from guajava leaves extract for controlling organophosphorus pesticides hazards, characterization, and in-vivo toxicity assessment, *BMC Pharmacol. Toxicol.*, 25(1), 98(2024). https://doi.org/10.1186/s40360-024-00826-7

Alshehri, A. A. and Malik, M. A., Phytomediated photo-induced green synthesis of silver nanoparticles using Matricaria chamomilla L. and its catalytic activity against rhodamine B, *Biomol.*, 10(12), 1–24(2020). https://doi.org/10.3390/biom10121604

Bala, A., Rani, G. and Ahlawat, R., Jatropha integerrima flower extract mediated green synthesis of silver nanoparticles: spectroscopic, catalytic, and antioxidant analysis, *Spectros. Lett.*, 55(10), 618–635(2022). https://doi.org/10.1080/00387010.2022.2137200

Bharadwaj, K. K., Rabha, B., Pati, S., Choudhury, B. K., Sarkar, T., Gogoi, S. K., Kakati, N., Baishya, D., Kari, Z. A. and Edinur, H. A., Green synthesis of silver nanoparticles using diospyros malabarica fruit extract and assessments of their antimicrobial, anticancer and catalytic reduction of 4-nitrophenol (4-np), *Nanomater.*, 11(8), 1999(2021). https://doi.org/10.3390/nano11081999

Biswas, K., Ahamed, Z., Dutta, T., Mallick, B., Biswas, P., Biswas, J. K. and Mandal, S. K., Bio-inspired formulation of starch-coated silver nanoparticles: A sustainable computing towards environmental monitoring and biomedical sectors, *Environ. Nanotechnol., Monitor. Managet.*, 25, 101118(2026). https://doi.org/10.1016/j.enmm.2025.101118

Boddu, S., Nagarjuna, K., Jajula, S., Kumar, V., Marri, B. P., Nagireddi, S. and Tondepu, S., Green Silver Nanoparticles: A Sustainable Approach for Photocatalytic Degradation of Rhodamine B, *J. Institut. Eng (India): Series D*, 105(3), 1989–1997(2024). https://doi.org/10.1007/s40033-023-00621-4

Chirumamilla, P., Dharavath, S. B. and Taduri, S., Eco-friendly Green Synthesis of Silver Nanoparticles from Leaf Extract of Solanum khasianum: Optical Properties and Biological Applications, *Appl. Biochem. Biotechnol.*, 195(1), 353–368(2023). https://doi.org/10.1007/s12010-022-04156-4

Dam, X. T., Nguyen, X. T., Nguyen, T. C., Nguyen, T. D., Duong, T. M., Bui, T. D. and Thai, H., Bio-Synthesis of Silver Nanoparticles Decorated on Hydrotalcite using *Psidium guajava* Leaf Extract and Its Anti-Bacterial Effect, *ChemistrySelect*, 9(8), e202303711(2024). https://doi.org/10.1002/slct.202303711

Dharavath, S. B., Maduru, N., Porika, M., Chirumamilla, P., Veera, S., Ponnam, N. and Taduri, S., Green synthesis of silver nanoparticles using Nothapodytes foetida leaf extract: Optical, antibacterial and anticancer activities, *Next Nanotechnol.*, 7, 100162(2025). https://doi.org/10.1016/j.nxnano.2025.100162

Gaddala, B., Devi, K. V, Balakrishnan, V., Sundramurthy, V. P., Hariprabhu, M., Mayakannan, S., Kadaikunnan, S. and Khaled, J. M., Evaluation of detoxification performance of Pithecellobium dulce seed pod

powder upon acid treatment: removal of reactive red 195-A dye and kinetic analysis, *Zeitschrift Fur Physikalische Chemie*, 239(6), 885–910(2025). https://doi.org/10.1515/zpch-2024-0879

Ganvir, H. V, Hadidi, H. M., Saminathan, R., Bhagat, M. S., Krishnaraj, C. and Satishkumar, P., Green Sol–gel Synthesis of $Cu/Co_3O_4$ Nanocomposite Using *Curcuma longa* Leaf Extract for Highperformance Supercapacitor Electrodes, *J. Environ. Nanotechnol.*, 15(1), 543–554(2026). https://doi.org/10.13074/jent.2026.03.2541993

Hachem, Z., Kashmar, R., Abdallah, A. M., Awad, R. and Khalil, M. I., Cyclamen libanoticum is a Novel Bioresource for Green Silver Nanoparticles with Antibacterial and Antioxidant Capabilities, *Curr. Nanosci.*, 21(4), 731–748(2025). https://doi.org/10.2174/0115734137310446240616164456

Hamadi, M. S., Hachem, Z., Abdallah, A. M., El-Sayed, A. F., Hamdalla, T. A., Khalil, M. I. and El Hajj, R., Green synthesis of silver and gadolinium doped nanoparticles from Ceratonia siliqua leaves extract: Characterization, antibacterial effect and molecular docking, *Hybrid Adv.*, 12, 100615(2026). https://doi.org/10.1016/j.hybadv.2026.100615

Hijazi, B. U., Faraj, M., Mhanna, R. and El-Dakdouki, M. H., Biosynthesis of silver nanoparticles as a reliable alternative for the catalytic degradation of organic dyes and antibacterial applications, *Curr. Res. Green Sustain. Chem.*, 8, 100408(2024). https://doi.org/10.1016/j.crgsc.2024.100408

Islam, M. J., Khatun, N., Bhuiyan, R. H., Sultana, S., Ali Shaikh, M. A., Amin Bitu, M. N., Chowdhury, F. and Islam, S., *Psidium guajava* leaf extract mediated green synthesis of silver nanoparticles and its application in antibacterial coatings, *RSC Adv.*, 13(28), 19164–19172(2023a). https://doi.org/10.1039/d3ra03381c

Islam, M. J., Khatun, N., Bhuiyan, R. H., Sultana, S., Ali Shaikh, M. A., Amin Bitu, M. N., Chowdhury, F. and Islam, S., *Psidium guajava* leaf extract mediated green synthesis of silver nanoparticles and its application in antibacterial coatings, *RSC Adv.*, 13(28), 19164–19172(2023b). https://doi.org/10.1039/d3ra03381c

Khan, A. N., Ali Aldowairy, N. N., Saad Alorfi, H. S., Aslam, M., Bawazir, W. A., Hameed, A. and Soomro, M. T., Excellent Antimicrobial, Antioxidant, and Catalytic Activities of Medicinal Plant Aqueous Leaf Extract Derived Silver Nanoparticles, *Processes*, 10(10), 1949 (2022). https://doi.org/10.3390/pr10101949

Khudhur, H. R., Abed, S. H., Sadaka, M. W. M., Mohammadalizadeh, M., Kadhim, S. A. and Shamkhi, A. F., Eco-friendly Synthesis of Plasmonic Silver Nanoparticles: Multifunctional Catalytic, Antimicrobial, Antioxidant, and Anticancer Activities, *Plasmonics*, 20(10), 8863–8877(2025). https://doi.org/10.1007/s11468-025-02783-1

Kim, B., Song, W. C., Park, S. Y. and Park, G., Green synthesis of silver and gold nanoparticles via sargassum serratifolium extract for catalytic reduction of organic dyes, *Catal.*, 11(3), 347(2021). https://doi.org/10.3390/catal11030347

Kute, M., Ghotekar, J., Baste, Y., Pagar, B., Waje, M., Kute, D. and Jadhav, V., Green synthesis of Ag-doped ZnO nanomaterials for photocatalytic, gas sensing, and antimicrobial activities: Insights from molecular docking, *J. Ind. Chem. Soc.*, 103(6), 102652 (2026). https://doi.org/10.1016/j.jics.2026.102652

Mani, M., Chang, J. H., Dhanesh Gandhi, A., Kayal Vizhi, D., Pavithra, S., Mohanraj, K., Mohanbabu, B., Babu, B., Balachandran, S. and Kumaresan, S., Environmental and biomedical applications of AgNPs synthesized using the aqueous extract of Solanum surattense leaf, *Inorg. Chem. Commun.*, 121, 108228(2020). https://doi.org/10.1016/j.inoche.2020.108228

Rehan, M., Nada, A. A., El-Maghrabi, H. H., Shaarawy, S., Abdel-Aziz, M. S. and Montaser, A. S., Eco-friendly biosynthesis of titanium dioxide/silver nanoparticles ($TiO_2$@Ag NPs) for multifunctional cotton fabrics with UV-protection, antimicrobial, catalytic, photocatalytic, and SERS activities, *J. Ind. Eng. Chem.*, 160, 486–521(2026). https://doi.org/10.1016/j.jiec.2026.01.059

Sahare, S. B., Satishkumar, P., Ramamurthy, S., Vijayan, D. S., Packirisamy, A. S. B., Prakash, R. and Krishnakumar, P., Investigation of the Mechanical and Morphological Behavior of Hybrid PALF-Kenaf Composites Reinforced with Hydroxyapatite and Zinc Oxide Nanoparticles, *J. Environ. Nanotechnol.*, 14(3), 443–453(2025). https://doi.org/10.13074/jent.2025.09.2531589

Segovia-Sandoval, S. J., Ojeda-Galván, H. J., Moral-Rodríguez, A. I., Rodríguez-Hernández, J., Peralta-Rodríguez, R. D., Gómez-Villegas, K. J., Hernández-Juárez, N. I. and Mendoza-Mendoza, E., A novel green synthesis of $Bi_2WO_6$-based photocatalysts for efficient pollutants degradation using low-power UV-A LEDs, *J. Alloys Compds.*, 911, 165018(2022). https://doi.org/10.1016/j.jallcom.2022.165018

Sharma, S., Devi, B., Koiri, D., Sharma, K., Bhattacharyya, K. G. and Devi, A., Visible light photocatalytic degradation of methylene blue and rhodamine B over silver-doped titanium dioxide nanocomposites supported on Fuller's earth, *Environ. Monitor. Assess.*, 195(11), 1362(2023). https://doi.org/10.1007/s10661-023-11981-5

Sharmiladevi, S., Ramesh, N., Prabhu, S. V and Mayakannan, S., Microwave-assisted functionalized biosorbent preparation using seed gum of Tamarindus indica: characterization and evaluation of Cr(VI) removal potency from tannery effluents, *Biomass Convers. Biorefin.*, 14(12), 13533–13545(2024). https://doi.org/10.1007/s13399-024-05667-2

Singh, J. and Dhaliwal, A. S., Synthesis of rGO/AgNPs adsorbent for the effective removal of two basic dyes:

kinetics, isotherms and thermodynamic studies, *Int. J. Environ. Sci. Technol.*, 20(10), 11483–11500(2023). https://doi.org/10.1007/s13762-022-04610-0

Sivalingam, A. M., Green synthesis and characterization of silver nanoparticles (AgNPs) using Bacopa monnieri leaf extract photoluminescence (PL) profiling and applications of antioxidant, antimicrobial activity, *Inorg. Chem. Commun.*, 184, 115898(2026). https://doi.org/10.1016/j.inoche.2025.115898

Sugumar, M., Bharathi, S., Sampath, V., Sundramurthy, V. P., Selvaraju, M., Kadaikunnan, S. and Khaled, J. M., Biosorption of Pb(II) ions through nanostructured teff straw based magnetized activated biocarbon: Aspects on modeling, optimization, and kinetics, *Global Nest J.,* 26(9), (2024). https://doi.org/10.30955/GNJ.06479

Vadivel, M., Hadidi, M. H., Saminathan, R., Bhagat, S. M. and Satishkumar, P., Synergistic $TiO_2$ Nanosheets and Nitrogen-doped Carbon-coated $NiCo_2O_4$ Nanocomposite for High-performance Hybrid Supercapacitors, *J. Environ. Nanotechnol.*, 15(1), 249–261(2026). https://doi.org/10.13074/jent.2026.03.2541992

Vankudoth, S., Dharavath, S., Veera, S., Maduru, N., Chada, R., Chirumamilla, P., Gopu, C. and Taduri, S., Green synthesis, characterization, photoluminescence and biological studies of silver nanoparticles from the leaf extract of Muntingia calabura, Biochem. Biophys. Res. Commun., 630, 143–150(2022). https://doi.org/10.1016/j.bbrc.2022.09.054

Warkad, S., Sangeetha Gowda K., R., Mirajkar, K. K., More, S. S., Mudhish, E. A., Mahnashi, M. H., Maashi, M. H., Shaikh, I. A., Khan, A. A., Muddapur, U. M., More, V. S., Khan, A. A. and Hussain, M. G., Green Synthesis of Silver Nanoparticles and Fluconazole Hybrid Nanoformulations for Managing Fusarium oxysporum Wilt Disease in Chickpea Plants, *ChemistrySelect*, 11(12), e04721(2026). https://doi.org/10.1002/slct.202504721